Tailoring the multiphase flow pattern of gas and liquid through micro-packed bed of pillars

Márquez, Nathalie; Moulijn, Jacob A.; Makkee, Michiel; Kreutzer, Michiel T.; Castaño, Pedro

DOI
10.1039/c9re00056a

Publication date
2019

Document Version
Final published version

Published in
Reaction Chemistry and Engineering

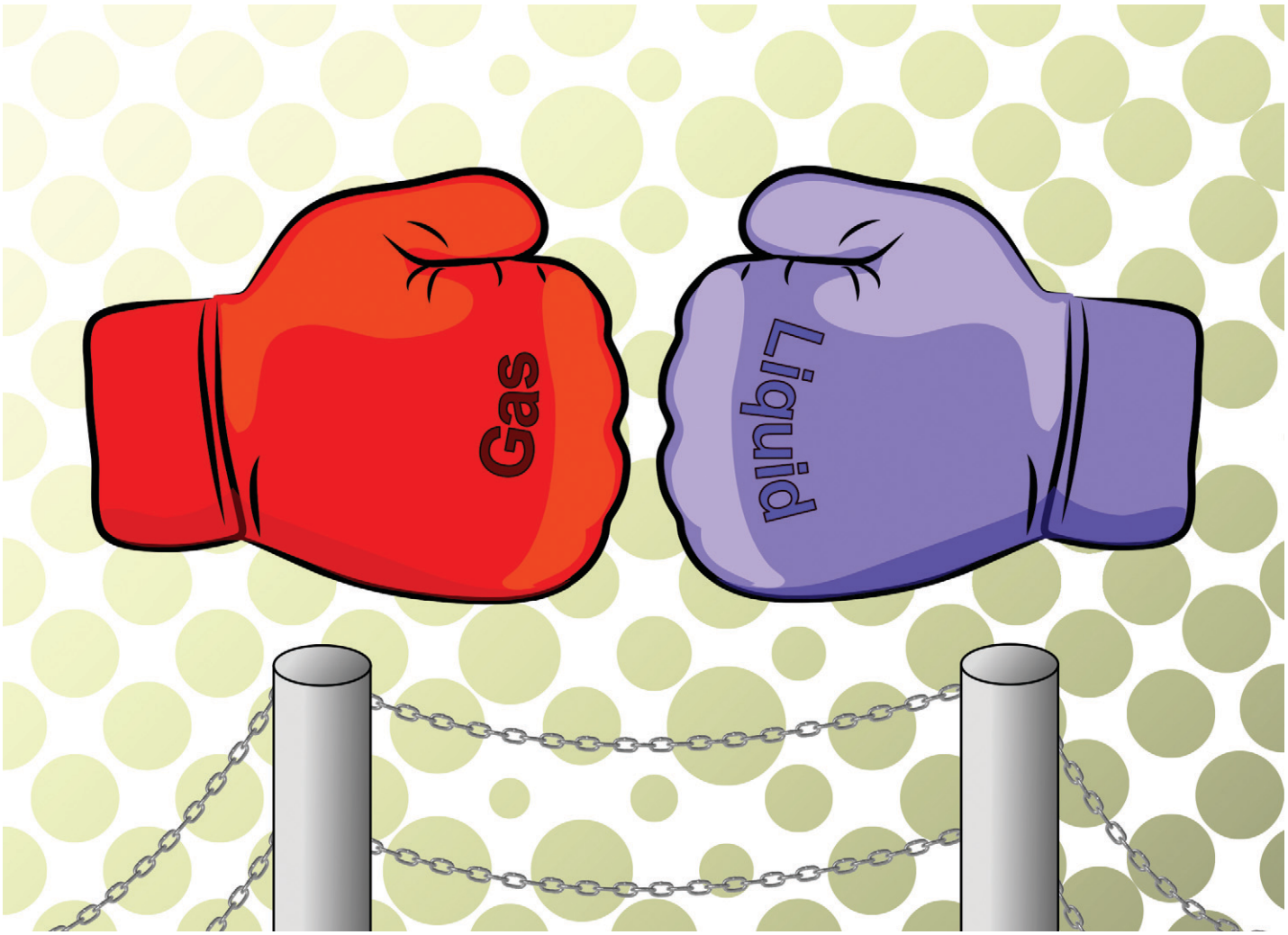

Showcasing research from Professor Castano's group; work mostly performed in the Catalysis Engineering Department, TUDelft, the Netherlands.

Tailoring the multiphase flow pattern of gas and liquid through micro-packed bed of pillars

The development of miniaturized multiphase reactors, driven for fast reaction screening, requires a fundamental understanding of the flow pattern within. In this work, we provide insights on how to control this flow pattern based on tuning the capillary number, contact angle or wettability and pillar arrangement.

As featured in:

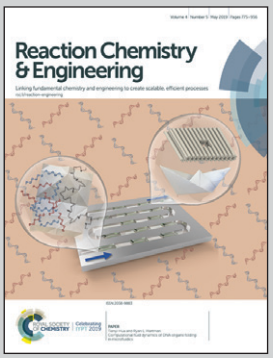

See Pedro Castaño *et al.*, *React. Chem. Eng.*, 2019, **4**, 838.

ROYAL SOCIETY OF CHEMISTRY | Celebrating IYPT 2019

rsc.li/reaction-engineering

Registered charity number: 207890

Reaction Chemistry & Engineering

PAPER

View Article Online
View Journal | View Issue

Cite this: *React. Chem. Eng.*, 2019, 4, 838

Tailoring the multiphase flow pattern of gas and liquid through micro-packed bed of pillars†

Nathalie Márquez,[a] Jacob A. Moulijn,[b] Michiel Makkee,[b] Michiel T. Kreutzer[c] and Pedro Castaño *[d]

Received 1st February 2019,
Accepted 29th March 2019

DOI: 10.1039/c9re00056a

rsc.li/reaction-engineering

We describe the co-current flow pattern of gas and liquid through micro-fabricated beds of solid and pillars under variable (i) capillary number, (ii) contact angle or wettability and (iii) pillar arrangement, *i.e.* modifying the distance between pillars or their size and comparing regular with more chaotic systems. Laser-induced fluorescent microscopy and image analysis are used to study the hydrodynamic interactions in terms of dynamics, liquid hold-up, and gas–liquid interfacial area per reactor volume. Those parameters provide insights into the multiphase flow patterns in these systems, how to control them, maximize mass transfer rate and unlock the potential of microreactors to reveal further intrinsic information.

Introduction

Multiphase micro-chemical systems take advantage of the large interfacial areas, fast mixing, and reduced mass- and heat-transfer limitations to achieve increased performance in comparison with conventional larger scale systems.[1] These features lead to platforms for fast screening of conditions and synthesis methods in what is known as flow chemistry.[2,3] In addition, the hydrodynamics are also affected by those size effects.[4–6] Micro-fabricated beds consist of channels with hydraulic diameters of the order of 100 μm and channels filled with stationary (sometimes porous) solids. These solids are arranged in a chaotic fashion by packing the bed with particles with a defined particle size distribution or in a regular fashion by fabricating posts or pillars inside the channel. These devices perform gas–liquid–solid reactions that benefit from the small volumes and an improved heat and/or mass transfer.[7–13] Kashid and Kiwi-Minsker[14] have reviewed the different potential applications of packed bed microreactors for gas–liquid–solid reactions.

When scaling down, the importance of surface forces increases, and the importance of body forces decreases.[15] The relative importance of the different forces such as gravity and inertia can be analysed using dimensionless numbers. The relative importance of gravitational stress with respect to surface tension is given by the Bond number (Bo), the relative importance of inertial stress with respect to surface tension is expressed by the Weber number (We), and the ratio of viscous stresses to surface tension is described by the capillary number (Ca). At low liquid and/or gas velocities and small channel size, viscous stress dominates over inertial stress, their ratio is given by the Reynolds number (Re). For multiphase (organic-gaseous and aqueous–gaseous) micro-fluidic systems at ambient pressure and temperature: $Bo < 10^{-3}$, $We < 10^{-5}$, and $Re < 10^{-2}$; therefore, gravitational and inertial stresses can be ignored. The flow is dominated by viscous stresses and the interfacial tension at the gas–liquid boundary, thus, the Ca number is the key parameter to predict the flow pattern.[16]

Günther and Kreutzer, summarized different experimental techniques for the characterization of micro-scale multiphase flow with the spatial and temporal measurement resolutions. Intrusive measurement probes are generally not an option for micro-fluidic systems. In the laser-induced fluorescence microscopy technique, the liquid phase is labeled with a fluorescent dye to reveal the gas–liquid distribution inside the device and the shape of the liquid interface. Yang *et al.*[17] have been able to use this approach and then to model the behavior of gas–liquid passing through a micro-packed bed of pillars by computational fluid dynamic (CFD) simulations of multiphase flow using the volume-of-fluid (VOF) method. The different modeling strategies for the multiscale phenomena in these systems have been reviewed by Ge *et al.*[18]

[a] *Avans University of Applied Sciences, School of Life Sciences and Environmental Technology, Lovensdijkstraat 61-63, P.O. Box 90.116, 4800 RA Breda, The Netherlands*
[b] *Catalysis Engineering, Department of Chemical Engineering, Faculty Applied Sciences, Technical University of Delft, Van der Maasweg 9, 2629 HZ Delft, The Netherlands*
[c] *Product and Process Engineering, Department of Chemical Engineering, Faculty Applied Sciences, Technical University of Delft, Van der Maasweg 9, 2629 HZ Delft, The Netherlands*
[d] *Department of Chemical Engineering, University of the Basque Country (UPV/EHU), P.O. Box 644, 48080, Bilbao, Spain. E-mail: pedro.castano@ehu.eus*
† Electronic supplementary information (ESI) available. See DOI: 10.1039/c9re00056a

As in large-scale systems, flow regime maps have been constructed for micro-packed beds that map flow patterns in a 2D domain of liquid and gas velocities.[19–21] However, by only using velocities, the effect of other parameters that can influence flow patterns, such as physical fluid properties[22] and inlet section design[23,24] are not reflected. The study of flow in porous media, relevant in oil recovery, has several common characteristics with the multiphase flow in micro-packed beds. Both the packing of particles and the channel filled with pillars can be analyzed as a connected network of void spaces or pores. In micro-fluidic systems involving micro-packed beds, channels filled with pillars and porous media the fluid velocities are low and surface forces are dominant: $Re < 10^{-2}$, $Bo < 10^{-2}$, $We < 10^{-6}$ and $Ca < 10^{-3}$.[25] The main difference in these systems is that oil-recovery studies are focused on the displacement of one phase by another (liquid for liquid or liquid for gas) and in packed beds for catalytic applications, gas and liquid phases have to flow together. Analysis of capillary pressure distribution in single channels with sinusoidal shape shows that surface-tension driven flow in such channels is controlled by the pressure extremes at their "crests" and "throats".[26] Oil recovery studies highlight the importance of the balance of pressures at the pore level.

The arrangement of the pillars or the 2D-3D disposition of the stationary solid material have proved to be extremely useful and important to tune the hydrodynamics in micro-reactors[27] or visualizing transport processes in porous systems.[28] The fact that the cylinders typically used in 2D systems are different to the particles used in 3D systems is a source of the high anisotropy observed for this kind of particle–fluid systems. In fact, anisotropy together with heterogeneity and nonlinear behavior are among the most evident features of the complexity of these systems.[18] Overall, little is known in regard to the effect of bed distortions on the hydrodynamic behavior of multiphase flow. Ferrari *et al.*[29] have shown that the heterogeneous geometries of pillars lead to a more dynamic flow behavior than homogeneous one for in porous media. Furthermore, the hydrodynamic behavior of microreactors is quite dynamical depending on the previous history.[30] Behavior that is also observed in porous media.[31] An uneven disposition of the solids within a microreactor can have a great effect on the hydrodynamics of micro-packed bed reactors.[32] At the same time, this earlier work[32] showed the potential of micro-fluidic devices to extract hydrodynamics behavior of microreactors aiming at high-throughput catalyst testing.

The goal of the current work is to describe the characteristics of the flow patterns observed in micro-packed beds at Ca numbers in the range 10^{-5}–10^{-3}. The dependence of the multiphase flow pattern in gas and liquid velocities, liquid viscosity, contact angle, and pore size are discussed, to get insight in the relevant parameters necessary for making flow pattern predictions. Ultimately, our purpose is to have a physical image of the flow pattern in miniaturized packed beds of cylindrical geometry (2 mm inner diameter) packed with spherical non-porous particles of about 100 μm (typically). For this aim, we have studied the impact of Ca number, contact angle, and pillar-array in the dynamics of the multiphase flow. The discussion of the results is in terms of the flow pattern observed, macroscopic liquid hold-up and gas–liquid interfacial area per reactor volume.

Experimental

Micro-packed bed design

The micro-packed bed system shown in Fig. 1a consists of independent gas and liquid feed ports, the bed section with the pillars array and one exit port. The gas feed passes through 50 μm wide serpentine channels with a significant pressure drop to assure a stable flow in the bed section.[33] We used before pressure drop measurements over micro-packed bed of particles to understand hold-up, transients and dispersion in these systems.[30,34] However, modelling and visualization in porous media shows that the local pressures over a micro-packed bed of pillars vary significantly across the bed.[35] De Loos *et al.*[36] has compared experimental results with different modelling approaches to calculate the pressure drop over a regular arrangement of pillars. These approaches cannot predict accurately the two-phase flow across the micro-packed bed of pillars. Nonetheless and taking into account the different porosities, viscosities and linear velocities, we can predict using his data that the pressure drop in this work is always $\ll 0.5$ bar.

The pillar-filled section is 60.0 mm long, 5.5 mm wide, and 70 μm high. In the basic design, it contains regular arrays of hexagonally positioned pillars. The pillars have a radius r of 60 μm and a centre-to-centre distance d_c of 150 μm. These dimensions were selected to have a bed porosity ε, defined as void volume divided by bed volume, of 0.42. As shown in the pillars array distribution in Fig. 1b and c, the positioning of the pillars relatively to the flow direction (y) avoids the formation of straight flow channels inside the bed.

To evaluate the influence of the bed width on the flow pattern, a second micro-packed bed system was made keeping all the dimensions of the original design constant but with a bed width of 3 mm. To study the effect of the size and position of pillars on the flow pattern (size of irregular void-channels), two additional micro-packed bed systems were designed. A third one with a pillar-array design that contains random deviations in the pillar position (pillar-centre coordinates $X_{i,j}$,$Y_{i,j}$) and constant pillar size (r = 60 μm) and a fourth design that contains random deviations in the pillar radius ($\gamma_{i,j}$) and constant pillar positioning (hexagonal array with centre-to-centre distance d_c = 150 μm). Fig. 1b shows the pillar-array without deviations. Fig. 1c gives an impression of the pillar-array when random deviations in both size and position of pillars are introduced.

According to Fig. 1 the following relations can be derived:

$$X_{i,j} = x_{i,j} + \omega_{xi,j} \quad (1)$$

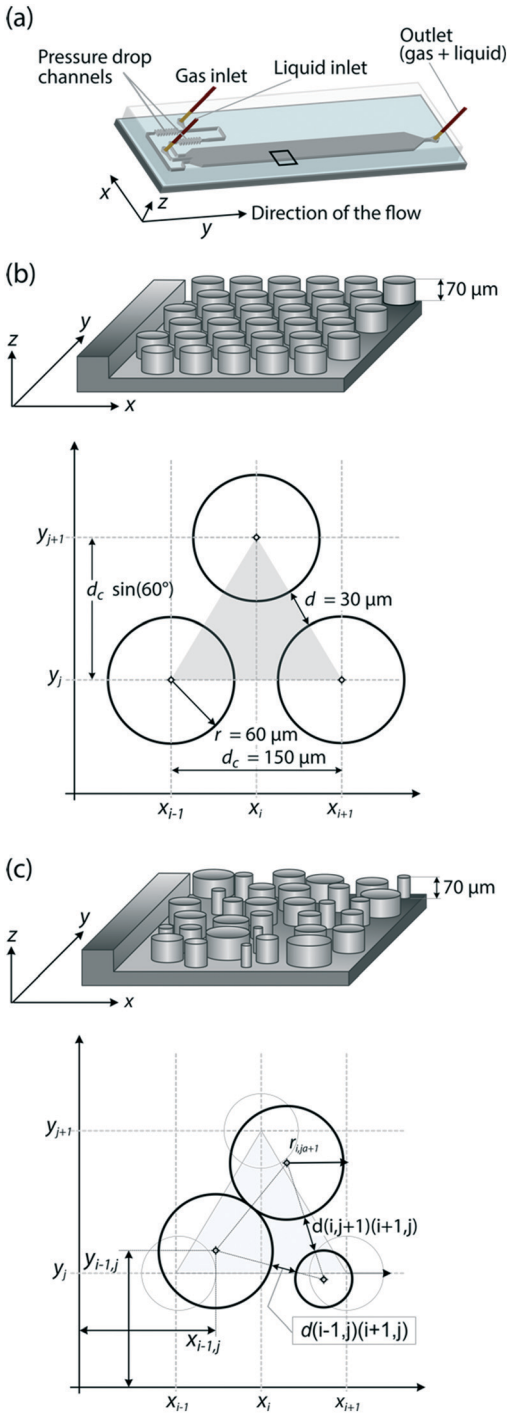

Fig. 1 (a) Micro-packed bed with inlets for gas or liquid and outlet, zoom of the pillar-array inside the device, and top view of the pillars distribution. (b) Pillar-array without random deviations. Hexagonal array with pillars of radius r = 60 μm, centre-to-centre distance d_c = 150 μm, and distance between two neighbouring pillars d = 30 μm. (c) Pillar-array with random deviations in terms of the pillar-centre coordinates ($X_{i,j}$,$Y_{i,j}$) and radius ($\gamma_{i,j}$). The pillars array is not hexagonal due to variations in the pillar-centre coordinates and the pillars have different sizes due to variations in the radius. Two neighbouring pillars can merge or touch, as shown.

$$Y_{i,j} = y_{i,j} + \omega_{yi,j} \quad (2)$$

$$\gamma_{i,j} = r_{i,j} + \omega_{ri,j} \quad (3)$$

$$d_c = |(x_{i-1}, y_j)(x_{i+1}, y_j)| = |(x_{i-1}, y_j)(x_i, y_{j+1})| = \ldots \quad (4)$$

$$d_{(i,j+1)(i+1,j)} = |(X_i, Y_{j+1})(X_{i+1}, Y_j)| - \gamma_{i,j+1} - \gamma_{i+1,j} \quad (5)$$

where $x_{i,j}$, $y_{i,j}$, and $r_{i,j}$ correspond to the pillar-centre coordinates and radius of the hexagonal array with centre-to-centre distance d_c = 150 μm and pillar radius r = 60 μm.

The random deviations (ω_x, ω_y, and ω_r) are produced using the Matlab function randn to generate a Gaussian distribution centred in zero with different standard deviations (σ_d for the variations in pillar position and σ_r for variations in pillar radius):

$$\omega_{xi,j} = (150\ \mu\text{m})\ \sigma_d\ (\text{randn}_{xi,j} - 0.5) \quad (6)$$

$$\omega_{yi,j} = (150\ \mu\text{m})\ \sigma_d\ (\text{randn}_{yi,j} - 0.5) \quad (7)$$

$$\omega_{ri,j} = (150\ \mu\text{m})\ \sigma_r\ (\text{randn}_{ri,j} - 0.5) \quad (8)$$

Table 1 illustrates, and Fig. 2 shows the main features of the designs studied in this work. Design 1 correspond to the standard arrangement and size, whereas design 2 corresponds to a narrower device. Designs 3 and 4 are related to irregular arrangement of pillars in position or size, respectively.

Fig. 2d Shows the normalized population of distances across pillars for designs 1, 3 and 4. Designs 1 and 2 have a unique distance between the pillars (30 μm, Fig. 1b) whereas designs 2 and 3 have certain degree of merge (distance = 0) and centred on a mean distance of ~30 and ~50 μm, respectively.

Fabrication process

The micro-packed bed systems were made of polydimethylsiloxane (PDMS) using standard soft-lithographic techniques. Silicon wafers were spin-coated with a layer of negative photo-resist SU-82050 (Microchem) at 3000 rpm. The thickness of the SU-8 layer was measured with an alpha-stepper at several locations across the wafer obtaining values between 75–105 μm. The designs of our micro-packed bed

Table 1 Relevant dimensions for the packed bed designs: bed width W, pillar radius r, pillar-centre distance d_c, standard deviation for the variations in pillar position σ_d, and standard deviations for variations in pillar radius σ_d. ε = 0.42

Design	W, mm	r, μm	d_c, μm	σ_d	σ_r
1	5.5	60	150	—	—
2	3.0	60	150	—	—
3	5.5	60	150[a]	0.25	—
4	5.5	60[a]	150	—	0.1

[a] Mean value.

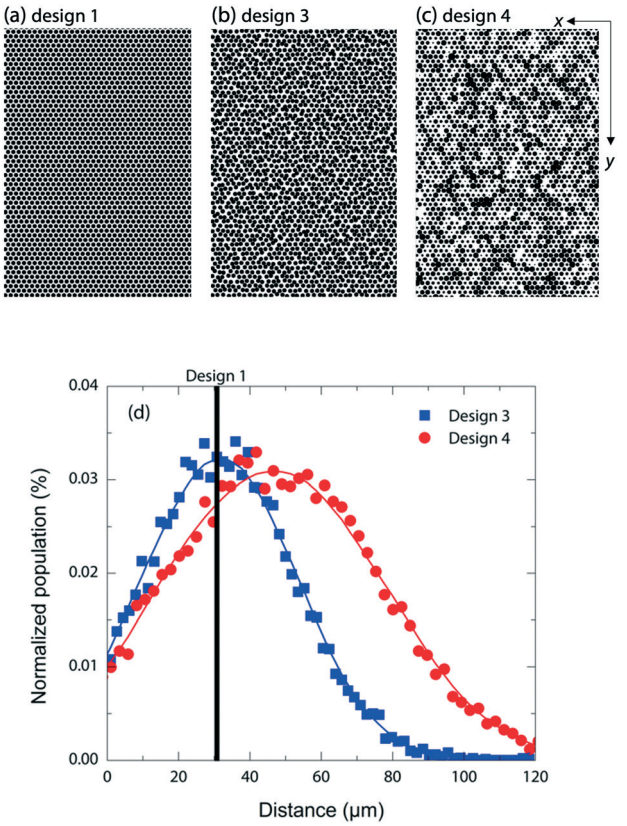

Fig. 2 Designs of the micro-packed beds corresponding to (a) design 1, constant pillars size of r is 60 μm and distance between pillars of d_c is 150 μm); (b) design 3, the pillar-centre coordinates $(X_{i,j},Y_{i,j})$ and therefore the pillar-centre distance d_c was varied; and (c) design 4: the pillars radius was varied keeping d_c constant. For designs 3 and 4, the distance between pillars can be negative, indicating merging of pillars. (d) Histograms showing the pillars distribution in the bed and the space between pillars. ε = 0.42.

systems were lithography transferred to the SU-8 layer using a transparency mask printed at 20 000 dpi. We mixed the PDMS pre-polymer and the curing agent (Sylgard 184 Silicone Elastomer Kit, Dow Corning) in a 1 : 10 weight ratio. Additionally, we added toner powder to the solution in a 1 : 60 weight ratio to make the PDMS black for improving image contrast in the experiments. After curing, the PDMS layer was removed from the SU-8 master and cut to size. Holes were punched for the fluid inlets and outlet. Afterwards, the PDMS structure and a microscope glass slide (MENZEL-GLASER, 76 mm × 26 mm) were exposed to oxygen plasma (Harrick, model PDC-002) and, subsequently, bonded. Unless otherwise noticed, the visualization experiments were performed in the same day the PDMS structure and the microscope glass slide are exposed to oxygen plasma in order to prevent recovery of the hydrophobicity of plasma-treated PDMS.[37] This material, PDMS, have shown to deform over certain pressures.[38] However, under the conditions employed in this work we can may expect that this deformation does not affect the main design features of the micro-packed beds.

Flow visualization

Ethanol or polyethylene glycol 200 (PEG-200) with a flow rate between 8.8 and 45 μL min^{-1} were fed to the micro-packed bed system by a syringe pump (Harvard PHD2000) and gas flows with a flow rate between 82 and 93 μL min^{-1} at standard conditions were supplied from a pressurized vessel and regulated with a needle valve (Porter, vcd-1000). These flow rates render values of superficial velocities typically encountered in micro-reactors for catalytic applications, such as the hydrotreatment of diesel to obtain a fuel with a sulphur lever of below 10 ppm. Rhodamine-B, a fluorescent dye, was added to the liquid to enhance contrast.

It is well accepted that the flow history has an impact on the final hydrodynamic behaviour of the multiphase flow through particles or pillars.[18] This history is related with the multiplicity of hydrodynamic states in trickle bed reactors.[39] Our previous experiments on micro-packed bed reactors showed that wet or dry start-up procedures resulted in the same hydrodynamic state after stabilization.[30] Thus, our experiments have started with liquid filling of the system for 15 min. We allowed the hydrodynamic behaviour to stabilize for at least 60 min after starting the flow of gas and before we started recording the images.

The flow was visualized through a 1× air objective mounted on an inverted epifluorescent microscope (Zeiss axiovert 200 M) equipped with a CCD camera (La Vision, Imager Intense). A mercury arc lamp was used, and images were recorded at frame rates of 2 or 4 Hz with an exposure time of 5 ms. No changes in the fluorescent micrographs with a higher frequency were observed, so the recorded movies at this frame rate captured all the dynamics of the flow. A series of these images (960 to 2000) cover a timescale of about 4 to 17 minutes, which was long enough to measure the dynamics of the flow. We used an objective of a relatively small magnification to visualize a relatively large area of the micro-packed bed system in order to correlate the flow structures in space. The flow was captured over the full width of the micro-packed bed and a length of 8 mm at several locations, covering the entire bed length.

The static contact angle of the liquid–solid (PDMS) interphase was measured with the sessile drop technique (Easy Drop DSA15S, Krűss).

Data processing

We used the fluorescent micrographs to calculate the local instantaneous liquid hold-up $\varepsilon_L(x,y,t)$ of the interstitial space between the pillars. The micrographs were binarized based on a threshold intensity. Each pixel in the channel with an intensity below the threshold is a pillar or a gas-filled zone and received a value $\varepsilon_L(x,y,t)$ = 0, while pixels with an intensity above the threshold were liquid filled and received a value $\varepsilon_L(x,y,t)$ = 1. In the images, the liquid phase is coloured white, while the gas phase and the pillars are coloured black.

The macroscopic liquid hold-up was calculated in an area that corresponds to the full width W of the micro-packed bed and a length ℓ of 8 mm as:

$$\varepsilon_{\mathrm{L,macroscopic}}(t) = \frac{1}{\varepsilon \cdot W \cdot \ell}\int_0^W \int_0^\ell \varepsilon_{\mathrm{L}}(x,y,t)\mathrm{d}x\mathrm{d}y \quad (9)$$

where ε is the bed porosity, defined as void volume divided by bed volume.

The macroscopic liquid hold-up averaged over time (for the same area) was calculated as:

$$\varepsilon_{\mathrm{L,ave}} = \frac{1}{t}\int_0^t \frac{1}{\varepsilon \cdot W \cdot \ell}\int_0^W \int_0^\ell \varepsilon_{\mathrm{L}}(x,y,t)\mathrm{d}x\mathrm{d}x\mathrm{d}t \quad (10)$$

The interstitial velocity was defined as the volumetric flow-rate of the phase divided by the available flow area for that phase:

$$u_{\mathrm{L}} = \frac{\varphi_{\mathrm{L}}}{W \cdot \ell \cdot \varepsilon \cdot \varepsilon_{\mathrm{L,ave}}} \quad (11)$$

$$u_{\mathrm{G}} = \frac{\varphi_{\mathrm{G}}}{W \cdot \ell \cdot \varepsilon \cdot \left(1-\varepsilon_{\mathrm{L,ave}}\right)} \quad (12)$$

The time-averaged local liquid hold-up at different cross-sections in the y direction (over a length ℓ of 8 mm) was calculated as:

$$\hat{\varepsilon}_{\mathrm{L}}(y) = \frac{1}{\varepsilon \cdot \ell}\int_0^t \int_0^\ell \varepsilon_{\mathrm{L}}(x,y,t)\mathrm{d}x\mathrm{d}t \quad (13)$$

For multiphase reactions, the gas–liquid interfacial area per reactor volume a was an important parameter for reactor performance. We estimated the interfacial area using an edge finding routine (*regionprops*) from Matlab (Version R2007b. The MathWorks, Inc., 2009). As depicted in Fig. 3, firstly we took a fluorescent micrograph, in this image the liquid-filled zones were made of white pixels and the gas and solid zones correspond to black pixels. Using the edge finding routine we detected the interfaces with the liquid (gas–liquid and solid–liquid). Secondly, we took an averaged image in which the light intensity of each pixels is the accumulated light intensity value of 500–1000 micrographs, this number of images was large enough to assume that all the voids have been wetted to at least some time, *i.e.* $\varepsilon_{\mathrm{L,ave}} > 0$. In the averaged image, a pixel corresponding to a solid or only gas zone will have an accumulated light intensity between 0 to 5% of the maximum accumulated value. This criterion was used to identify a solid or only gas zone.

As described in Fig. 3, we binarized this averaged image and used the edge finding routine we determine the solid–liquid interface. Subsequently, we subtracted the number of pixels that form the solid–liquid interface to the number of pixels of interfacial area from the fluorescent micrograph (gas–liquid and solid–liquid). This methodology has proved useful for porous media data treatment.[40] In this way we calculated the number of pixels of the gas–liquid interfacial perimeter. Since the height of the micro device is constant (70 μm), a was calculated as the ratio of interfacial perimeter per bed area. The bed area was the sum of all the pixels that formed the micrograph (typically *ca.* 459 × 352). It is worth mentioning that using this technique; completely stagnant gas zones were considered pillars. The results reported by Yin *et al.*[41] enable to predict that the interphase is approximately vertical across the thickness of the chamber.

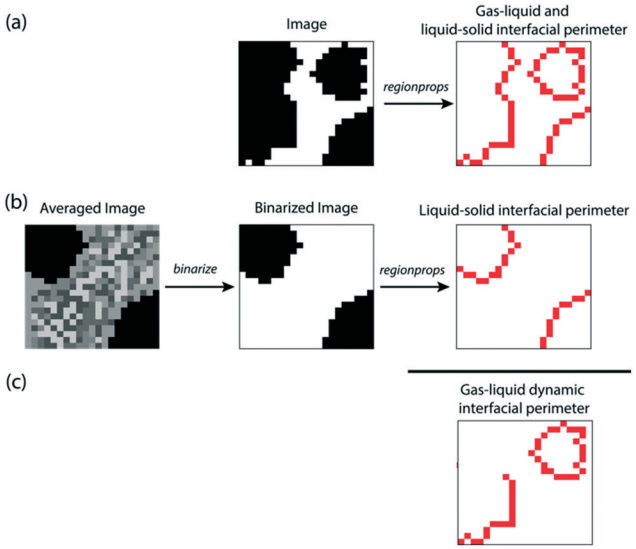

Fig. 3 Schematic representation of the gas–liquid interfacial perimeter calculation. (a) Firstly, we determine the gas–liquid and liquid–solid interfaces with a micrograph and an edge finding routine. (b) Secondly, we determine the liquid solid interface binarizing an averaged image; this is our reference for identifying the pillars. (c) Finally, we subtract the number of interfacial pixels of the reference from the number of interfacial pixels of the image to get the number of pixels for the gas–liquid interfacial perimeter.

Results and discussion

Effect of fluid properties – capillary number

The effects of fluid properties on the flow pattern were visualized in the bed with the regular pillar distribution (design 1). Ethanol and PEG-200 were used as liquids, varying in this way the liquid viscosity and the interfacial tension. To achieve larger gas and liquid velocities at the same flow rates, air and ethanol were flown over a bed with a regular pillars distribution but a narrower width (design 2). The relevant fluid properties for these experiments are depicted in Table 2.

In the sequence of micrographs shown in Fig. 4, the black circles represent the pillars, the black zones represent the gas-filled areas and the light zones are liquid-filled. The flow direction of both phases, gas and liquid, is from left to right. Fig. 4a corresponds to micro-fluidic design 1, with ethanol and air as the working fluids and a bed width of 5.5 mm (Ca

Table 2 Relevant fluid properties for experiments made in micro-packed beds with a regular pillar-array. The first two columns describe the micro-packed bed system used and the working liquid, third and fourth columns show the relevant fluid properties estimated at 302 K (Handbook chemistry and physics web edition),[42] fifth column shows the macroscopic liquid hold-up averaged over time (calculated according to eqn (10)), sixth and seventh columns show the interstitial velocities, and the last column shows the capillary number Ca based on the liquid phase

Design	Liquid	η_L, mPa s	σ, mN m^{-1}	$\varepsilon_{L,ave}$	u_L, mm s^{-1}	u_G, mm s^{-1}	Ca
1	Ethanol	1.0	22	0.58	1.6	25.8	7.64×10^{-5}
2	Ethanol	1.0	22	0.65	2.7	52.7	1.25×10^{-4}
1	PEG-200	37.7	44	0.61	1.6	25.8	1.35×10^{-3}
1	PEG-200	37.7	44	0.80	6.0	50.3	5.16×10^{-3}

$= 7.64 \times 10^{-5}$). As could be appreciated, all the micrographs look almost the same in the time interval of 4 min. There are preferential paths for each phase and the interface hardly moves. Thus, the flow is segregated. To a first approximation, the liquid flow might be regarded as bound by stationary boundaries of gas or solid. Hence, the flow of liquid is hardly perturbed by the gas flow. In other words, the hydrodynamic interaction between the two phases is minimal. Fig. 4b corresponds to micro-fluidic design 2 (reduced bed width), for this case the ethanol and air velocities are roughly two times higher than that in the previous case. These higher velocities produce a much more dynamic flow pattern. The gas moves through the bed as "snakes" that change form and position in a time interval of seconds in a liquid-filled medium. In contrast to the flow in design 1, in this case the interaction between gas and liquid flow is significant. This flow pattern

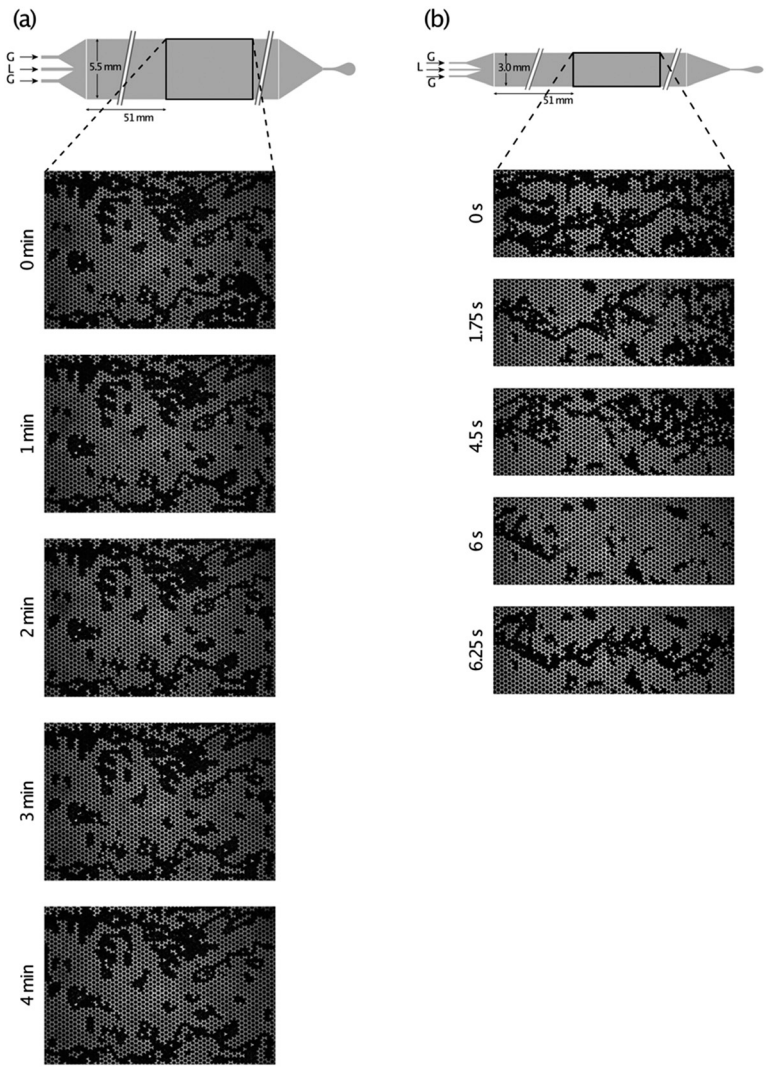

Fig. 4 Sequence of images to illustrate the flow dynamics encountered in micro-packed beds with a regular pillar-array at different ethanol and air velocities. a) u_L = 1.6 mm s^{-1}, u_G = 25.8 mm s^{-1}. b) u_L = 2.7 mm s^{-1}, u_G = 52.7 mm s^{-1}. A video of the sequence (b) is provided as ESI.

was defined as "snake flow". A snake of gas can expand over up to 5 pillars over the channel-width; this indicates that the snakes-width is around 640 μm. A video of the corresponding snake flow in design 2 is provided as ESI.† This inestable snake flow is named "viscous fingering" or "Saffman–Taylor instability" in the porous media literature,[43] where it is considered detrimental for fluid displacement.[44] However, in our case this instability is beneficial because it enhances mixing and decreases the impact of external mass transfer.

Comparing our results within the flow map of Wada *et al.*,[19] it is clear that the flow pattern they predict for both cases is very different for what we have described: slug flow with gas plugs of the size of the channel width passing through a continuous liquid phase. The visualization experiments of Wada *et al.*[19] were done with oxygen and ethyl acetate for the same velocities of our experiments; their Ca numbers are both of the order of 10^{-5} which is the same order of magnitude of the Ca number of the flow dynamics as encountered in Fig. 4a. Evidently, the Ca number is not the only parameter predicting the flow pattern in a micro-packed bed, other parameters play also a role. It is worth mentioning that the feed section design of these authors is very similar to ours, but the dimensions of the bed are different, with a ratio of width: height of 2 (600 μm/300 μm) in comparison to a ratio of 78 (5500 μm/70 μm) for the work presented here. It is worth mentioning that the width of the snakes (640 μm) observed in Fig. 4b are very similar to the width of the gas plugs (600 μm) observed by Wada *et al.*,[19] but for our experiment the Ca number is one order of magnitude larger (1.25×10^{-4}). Additionally, their bed is made of 50 μm diameter pillars with a pillar-centre distance of 110 μm. This gives roughly a 60 μm width channel between pillars, which is a factor of 2 larger than the space available between pillars in the bed used for this work. For low capillary values, the movement of gas–liquid interfaces is dominated by the Laplace pressure jump across the interface; therefore, the size of the passages between pillars has a large effect in the flow patterns obtained. As described before,[37] the contact angle is another factor to consider when predicting flow patterns in micro-devices.[37] Unfortunately, Wada *et al.*[19] did not report the contact angle of their experiments. They reported that all surfaces in contact with reacting fluids had characteristics similar to those of glassware. Recently, Yang *et al.*[17] reported results obtained with a similar pillar arrangement. Their predictions agree with our results.

Fig. 5a corresponds to micro-fluidic design 1 with PEG-200 and air as the working fluids and a bed width of 5.5 mm. When using PEG-200, Ca = 1.35×10^{-3}, this value is 18 times larger than that when comparable flow rates are used with ethanol and air (Fig. 4a); therefore, viscous forces are relatively more important for this case. As expected, the gas phase moves as dispersed slugs in a continuous liquid phase. The gas bubbles that move across the bed, in a time-scale of seconds, encompasses three or more micro-pillars. This is known as churn flow, which at the same time is associated with the largest interfacial areas.[17]

Our results are analogous to those of Krishnamurthy and Peles[22] on their gas and liquid flow across micro-pillars. For $u_G < 1$ m s^{-1} they observed bubbly slug flow. Bubbles were defined as dispersed gas in the liquid with characteristic size less than or equal to the inter-pillars space. Their micro-channel is 1500 μm wide, 1 cm long, and 100 μm high, encompassing 68 alternating rows of 9 and 10 staggered circular 100 μm diameter pillars. At lower surface tension of the liquid phase (that is, higher Ca) gas slugs were shorter and the size of the bubbles smaller. In our experiments we did not see bubbles, but we can conclude that due to the higher viscosity, the gas snakes of Fig. 4a are shortened to gas slugs. This conclusion is in agreement with the previous modelling performed on slugs in microchannels.[45] At the same time, the channelling effect of gas within the micro-packed bed can lead to a serious by-passing of volatile species within the liquid medium.[46]

Fig. 5b corresponds to micro-fluidic design 1 with a five times larger PEG-flow-rate in the 5.5 mm-width bed. The larger liquid velocity produces a flow pattern that resembles reverse annular flow, where the liquid flows preferentially in the middle and gas slugs travel towards the edges. The gas/liquid distribution is very stable, as can be seen in the different micrographs with a time interval of 1 min. We conclude that this flow pattern is a consequence of the inlet design, because the liquid is fed in the middle, and in all the cases the liquid zone appears in the middle. The flow conditions at the inlet are far from equilibrium, but far downstream the inlet section (after 51 mm), the effect tends to disappear. We did not observe a variation of the transverse distribution with length in our work.

Fig. 6a shows the macroscopic liquid hold-up values averaged over the full width of the micro-packed bed. These values are similar to those of micro-packed beds arranged chaotically.[34] The segregated and reverse annular flow patterns (design 1 with ethanol and PEG-200 with a high liquid-to-gas ratio) have a relatively constant macroscopic liquid hold-up value while the flow patterns with gas snakes or slugs show some oscillations. It is worth mentioning that, in general, the liquid hold-up values are large in comparison to those of industrial and laboratory trickle-bed reactors. For larger scale reactors the largest liquid hold-up values are achieved when the bed is diluted with smaller particles as reported by Kulkarni *et al.*,[47] who found an increase liquid hold-up value from about 0.05 to 0.25 upon dilution of a bed packed with 6 mm glass spheres with 0.2 mm glass particles. The values reported in this work are larger than those by at least a factor of 2, obviously because surface tension dominates over gravitational stress (Bo $< 10^{-3}$).

The local distribution of the time-averaged liquid hold-up is shown in greater detail in Fig. 6b–e. The ideal situation would be a homogeneous value in the whole bed, *i.e.* gas slugs homogeneously distributed in the whole bed. This ideal situation is only observed in Fig. 6d (PEG-200 and air, Ca = 1.35×10^{-3}). In Fig. 6b and e, the gas flows preferentially on the wall, reducing the liquid hold-up in those areas. In Fig. 6c, the two-lateral gas-

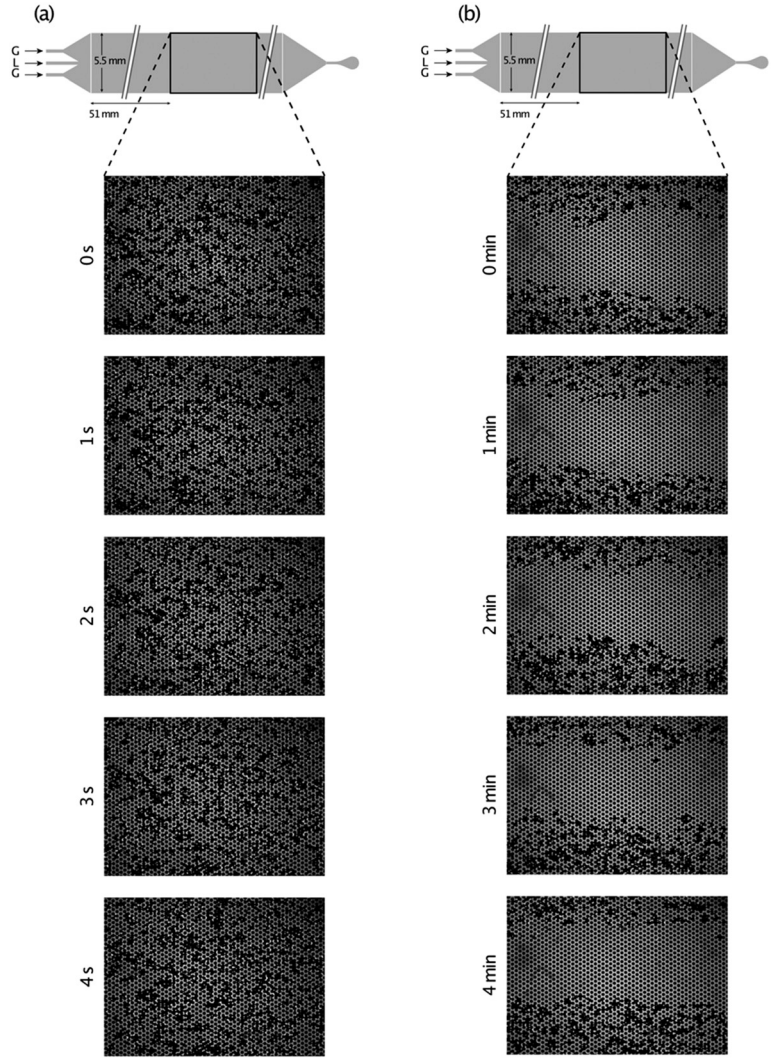

Fig. 5 Sequence of images to illustrate the flow dynamics encountered in micro-packed beds with a regular pillar-array at different polyethylene glycol 200 (PEG-200) and air velocities. a) u_L = 1.6 mm s^{-1}, u_G = 25.8 mm s^{-1}. b) u_L = 6.0 mm s^{-1}, u_G = 50.3 mm s^{-1}.

feed lines are closer than that in the other cases due to the smaller bed width (3.0 mm); therefore, the two gas branches merge into a single one that passes throughout the centre. That is to say, the flow pattern observed is the result of the inlet design.

Fig. 6f shows the averaged gas–liquid interfacial area per reactor volume (a). For the micro-fluidic design 1 with PEG-200 and air, Ca = 1.35 × 10^{-3}, the area (a) is at his highest value and a homogeneous liquid hold-up value in the whole bed is observed (Fig. 6d). This flow pattern is ideal to limit the impact of mass transfer limitations because it combines good solid wetting, high gas–liquid interface, and short diffusion-lengths. The other flow patterns have lower gas–liquid interfacial values due to a higher degree of segregation of the phases, which is combined with uneven liquid hold-up distributions; therefore, they are less attractive to minimize mass transfer. With the procedure used in this work to calculate a, it is not possible to discriminate solid areas from only gas zones; therefore, our solid–liquid interfacial perimeter calculation also includes some gas–liquid interface.

For the different flow regimes observed in this work, the interfacial areas are one order of magnitude larger than typical values for trickle beds with particles in the mm range.[48] Using Midoux's correlation,[49] for 1.5 mm particles in the trickling flow regime, the calculated gas–liquid interfacial area is 713 m^{-1}. For micro-packed beds, Losey *et al.*[7] reported a gas–liquid interfacial contact area of 16 000 m^{-1} for what they called dispersed flow, and Wilhite *et al.*[21] estimated gas–liquid interfacial area values between 1100 and 2400 m^{-1} assuming purely annular flow. For our reverse annular flow, we calculated an interfacial area of 3000 m^{-1}; therefore, the order of magnitude of our results is in the right range when compared with other micro-packed beds.

Effect of solid properties – contact angle or wettability

The wettability of a solid can be quantified by the contact angle, *i.e.*, the angle of inclination of the liquid–gas interface at the triple line (liquid–gas–solid).[50] As described in the

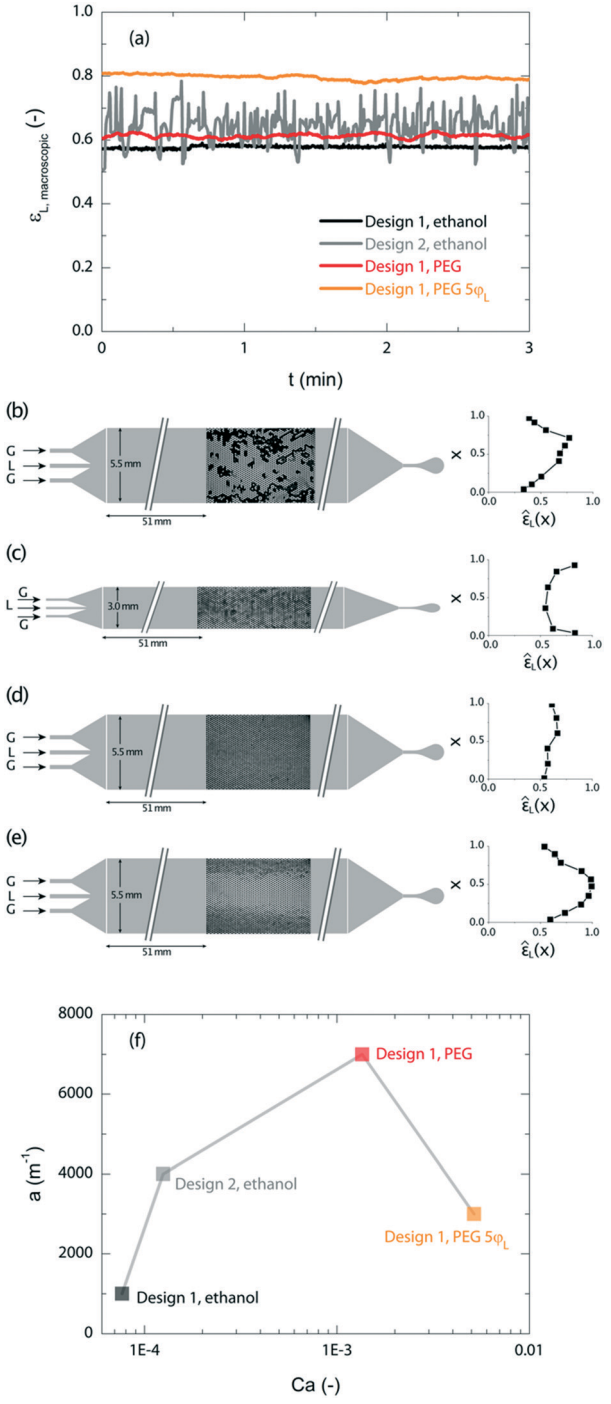

Fig. 6 a) Local liquid hold-up values *versus* time for the different designs and liquids used. The macroscopic liquid hold-up values are averaged over an area that corresponds to the full width of the micro-packed bed and a length of 8 mm, located at 51 mm downstream of the feed section. b–e) Micrographs showing the averaged local liquid hold-up over a period of four minutes in micro-packed beds with a regular pillar-array. Conditions: b) ethanol and air, u_L = 1.6 mm s^{-1}, u_G = 25.8 mm s^{-1}; c) ethanol and air, u_L = 2.7 mm s^{-1}, u_G = 52.7 mm s^{-1}; d) PEG-200 and air, u_L = 1.6 mm s^{-1}, u_G = 25.8 mm s^{-1}; e) PEG-200 and air, u_L = 6.0 mm s^{-1}, u_G = 50.3 mm s^{-1}; f) time-averaged gas–liquid interfacial area per reactor volume for the designs and liquids used corresponding to the same conditions shown before.

experimental section, the PDMS layer with the micro-fluidic design is bonded to a glass slide after exposing to oxygen plasma; thus, one wall of the device is made of glass. The surface properties of PDMS are (temporary) modified due to the exposure to oxygen plasma. The attack by oxygen radicals creates highly polar, hydrophilic groups at the PDMS surface that significantly alter the wetting properties, making the PDMS surface hydrophilic. Berejnov *et al.*[37] reported that when exposed to air at room temperature, the PDMS reverts to its natural hydrophobic state in a time scale on the order of days.

To assure a reproducible hydrophilic PDMS state, all the experiments were done within 4 h after exposure to the oxygen plasma. Each experiment last 1 hour and the surface properties could be considered constant during the experiment. The static contact angle of the air-ethanol-plasma treated PDMS is 6 ± 1°. The ethanol solution used for the static contact angle measurement is the same one as we used for our flow-visualization experiments (ethanol spike with rhodamine-B). The surface properties of the microscope glass slide are also altered by the oxygen plasma, but a precise analysis of surface energies after plasma is not needed because ethanol fully wets plasma-exposed glass.

After ten days, the PDMS had recovered its natural hydrophobic state with a static air–ethanol-PDMS contact angle of 34.7 ± 0.7°. To evaluate the effect of the contact angle in the flow pattern, ethanol and air were fed to the hexagonal pillar array in the 5.5 mm wide bed (micro-fluidic design 1) in the hydrophobic state (34.7°) at the same gas and liquid flows that render a segregated flow pattern under hydrophilic conditions (contact angle of 6°, Fig. 4a). As shown in the micrographs of Fig. 7, a change from hydrophilic to hydrophobic state (corresponds a change from complete wetting to partial wetting conditions) results in a change in the flow pattern: from segregated (Fig. 4a) to alternating slugs of liquids (Fig. 7), with approximately 6 Hz frequency, which completely fill the available area for flow. After the liquid slug is pushed away, the same gas and liquid distribution remains. This indicates the presence of stagnant zones. This slug pattern is more in the line of the flow pattern predicted by the 2D flow map of Wada *et al.*[19]

Fig. 8 shows the comparison in the flow patterns for the two gas–liquid–solid contact angles. Under partial wetting the anchoring process of the liquid–solid contact line is random.[51] When flowing gas and liquid, the intermittent adhesion of the liquid-film to the solid wall allows the formation of triple-lines. The liquid film can de-wet by nucleation and growth of dry patches. The contact lines increase the flow resistance.[52] Therefore, in the case of the channel filled with pillars, under partial wetting conditions many contact triple lines are formed, increasing the flow resistance. This would favour the local liquid accumulation until the local accumulated pressure is large enough to overcome the flow resistance. This process may lead to the formation of liquid slugs. For the PDMS in its natural hydrophobic state (contact angle = 34.7°), the macroscopic liquid holdup reaches very high

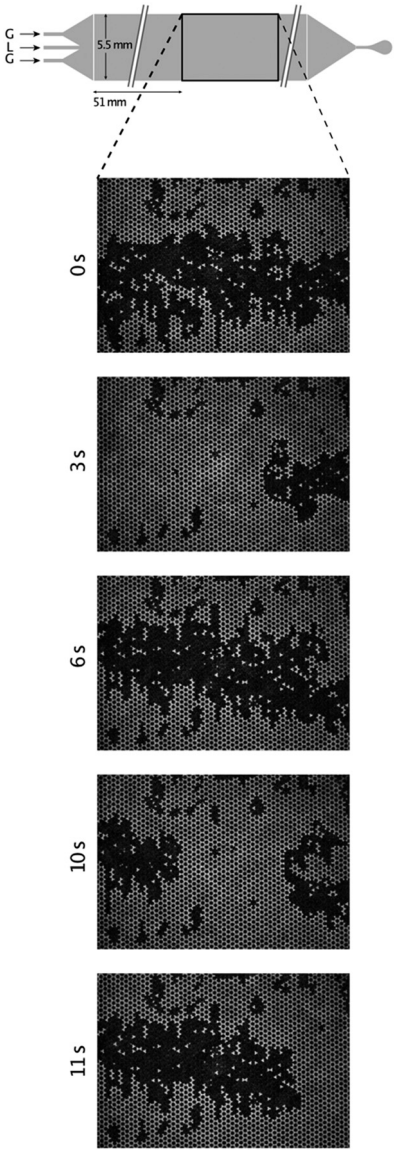

Fig. 7 Sequence of images to illustrate the flow dynamics (passage of liquid slugs) encountered in a micro-packed bed with a regular pillar-array at a static air–ethanol-PDMS contact angle of 34.7 ± 0.7° (hydrophobic state). Ethanol and air, u_L = 1.6 mm s^{-1}, u_G = 25.8 mm s^{-1}.

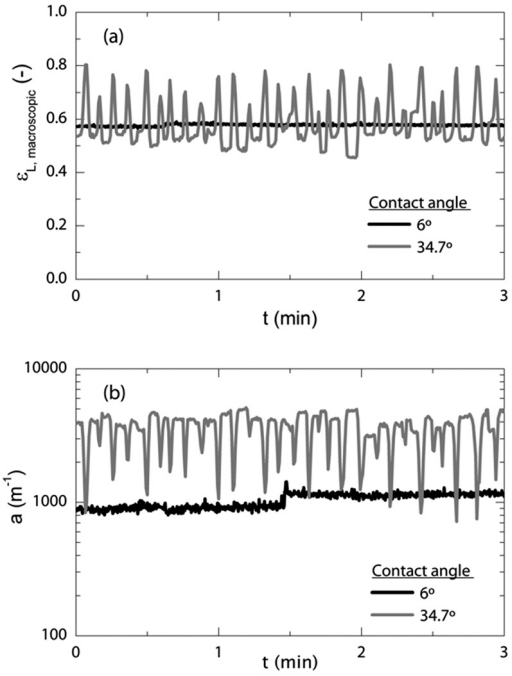

Fig. 8 a) Comparison of the liquid hold-up for different gas–liquid–solid contact angle. Macroscopic liquid hold-up as a function of time in a zone that corresponds to the full width of the micro-packed bed (5.5 mm) and a length of 8 mm. u_L = 1.6 mm s^{-1}, u_G = 25.8 mm s^{-1}. b) Comparison of the gas–liquid interfacial area, as calculated using the edge finding routine for different gas–liquid–solid contact angle. u_L = 1.6 mm s^{-1}, u_G = 25.8 mm s^{-1}.

values (~0.8) at the passage of a liquid slug. In the slug-regime the gas–liquid interfacial area is four times larger than that in the segregated flow pattern reducing its value at the passage of a liquid slug. These results indicate that in the slug regime there is more area for exchange between gas and liquid in comparison to the one in the segregated flow pattern. Our observations show a resemblance to porous media literature on the effect of contact angle.[53]

Effect of solid properties – pillar arrangement

The same air and ethanol linear velocities (u_L = 1.6 mm s^{-1}, u_G = 25.8 mm s^{-1}) were used in micro-fluidic designs 1, 3, and 4 (Tables 1 and 2) to evaluate the influence of deviations in the pillar-centre coordinates $(X_{i,j},Y_{i,j})$ and deviations in the pillar-radius in the flow pattern observed. For the three cases the bed dimensions are constant (60.0 mm long, 5.5 mm wide, and 70 μm high). The resulting sequence of images of designs 3 and 4 are shown in Fig. 9.

As it was earlier shown in Fig. 4a and averaged in Fig. 10a, for the regular pillar-array (design 1) the flow is segregated, and each phase has an almost constant preferential path in the bed with very low interaction between the phases. For the pillar-array of design 3 (Fig. 10b), with variations in the pillar-centre distance, the gas phase moves through the bed as snakes that change form and position in a variable frequency between 0.002–0.026 Hz. For the pillar-array of design 4 (Fig. 10c), with variations in the pillar radius, the area covered by the gas snakes is invaded by liquid during time intervals of *ca.* 2 s with a frequency of around 0.08 Hz.

Fig. 10d shows the averaged distribution of the liquid hold-up over a representative period of time. In Fig. 10a the phases are segregated with almost no interaction; therefore, we find, besides the pillar-region, only liquid-filled zones (white zones) and only gas-filled zones (black zones). In Fig. 10b, the gas-filled preferential paths or snakes change form and position leading to zones that are filled by both phases in an alternating way. Because of the slow frequency of the snake changes, we recorded images for a longer period of time (17 min) to have a good representation of the long-term behaviour. In Fig. 10c, as described before, part of the gas-filled zone is

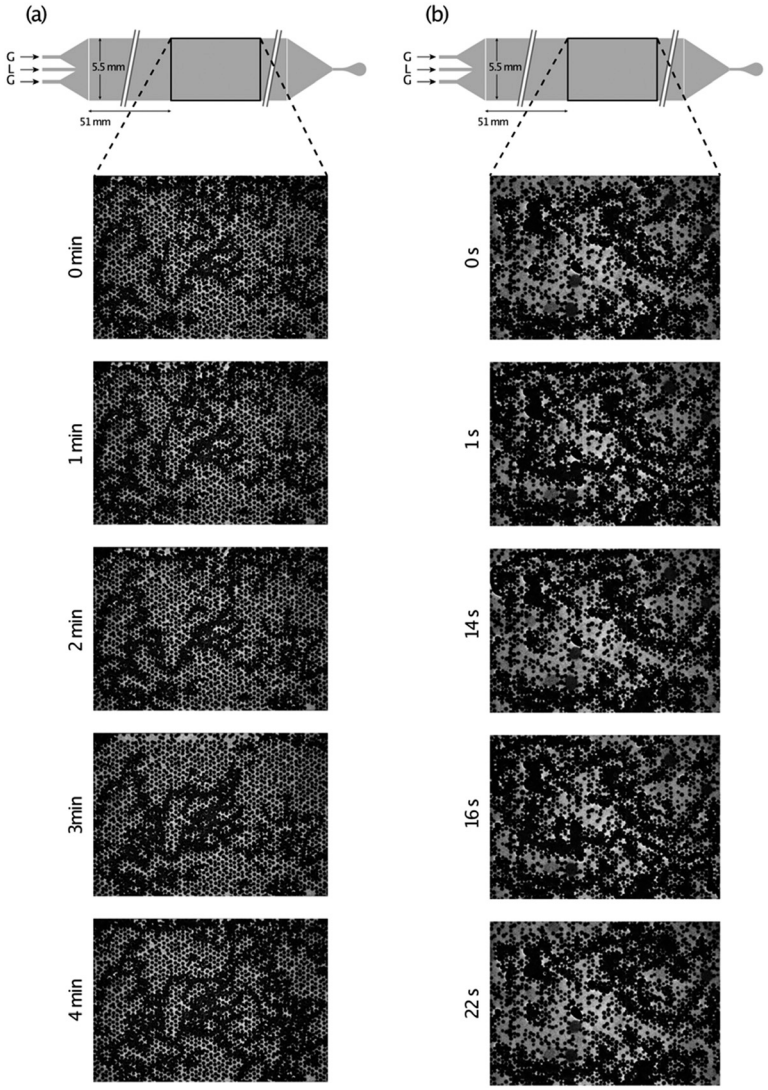

Fig. 9 Sequence of images to illustrate the flow dynamics encountered at same air and ethanol flow-rates in beds with different pillars size and distribution. a) Design 3 with variations in the pillar-centre coordinates ($X_{i,j}$,$Y_{i,j}$) and, therefore, in the pillar-centre distance d_c; b) design 4 with variations in the pillars radius and constant d_c. u_L = 1.6 mm s^{-1}, u_G = 25.8 mm s^{-1}.

invaded by liquid with a frequency of 0.08 Hz but almost 80% of the analysed area (5.5 mm × 8 mm) presents only gas and only liquid-filled zones. Images were recorded for 8 min.

Fig. 10d shows that designs 1 and 3 are very stable with a comparable level of macroscopic liquid hold-up values. For design 4, the liquid hold-up value peaks rather regularly, obviously due to the passing of a liquid slug. The result of design 4 resembles the result obtained with partial wetting conditions, where also liquid slugs were formed (Fig. 8a), but in the case of partial wetting, the slug frequency is higher, and the macroscopic liquid hold-up value reached is larger (~0.8). Fig. 10e shows that the gas–liquid interfacial area increases with variable inter-pillar space. As shown in Fig. 2d, the range of variations in pillar spacing is larger for design 4 than that for the distribution of design 3. Interestingly, design 3 presents a larger gas–liquid interfacial area when compared with designs 1 and 4. The gas–liquid interfacial area for design 4 decreases when a liquid slug passes in a similar way as the comparable result for partial wetting condition in Fig. 8b. These results indicate that the best scenario (for having the highest gas–liquid interfacial area) is the one corresponding to the homogeneous distribution of phases and hold-up across the micro-packed bed of pillars.

As a general observation, we have seen that the liquid tends to pass through the smaller voids between pillars while the gas tends to pass through the largest void-channels. Results from designs 1, 3, and 4 indicate that there is an optimum pillar-spacing range where the passages between pillars are occupied by both phases in an alternating fashion (design 3). Our results resemble those of Serres *et al.*[54] who compared spherical beads *versus* open cell solid foams obtaining better mass transfer within the former system. Serres *et al.*[55] and Arbabi *et al.*[56] also demonstrated the formation of Taylor gas bubbles across irregular 3D packings, as shown in Fig. 7.

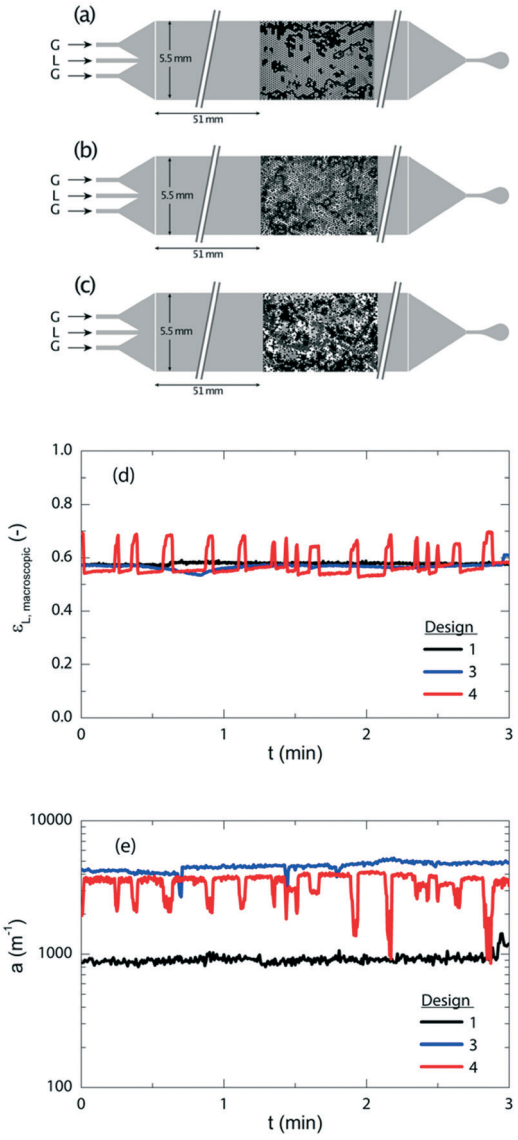

Fig. 10 a–c) Micrographs showing the time-averaged liquid hold-up over a representative period of time for the flow patterns encountered with same air- and ethanol-flow-rates in beds with different pillars size and distribution. a) Pillar-array with regular pillar size and position (design 1, same as show in Fig. 6b), averaged over 4 min; b) pillar-array with deviations in the pillar-centre distance, averaged over seventeen min; c) pillar-array with deviations in the pillar radius, averaged over 8 min. d) Macroscopic liquid hold-up and gas–liquid interfacial area per reactor volume for the flow patterns encountered with same air- and ethanol flow-rates in beds with different pillars size and distribution. d) Macroscopic liquid hold-ups in time; e) gas–liquid interfacial area per reactor volume. e) Gas–liquid interfacial area per reactor volume (*a*) at the same air- and ethanol flow-rates in beds with different pillars size and distribution.

Our observations are in good agreement with the porous media literature,[26,57] where it is described that the movement of gas–liquid interfaces is dominated by the capillary pressure jump across the interface. The inter-pillar pores can be described as channels of non-constant hydraulic diameter with throats and crests. In the zones inside the bed with smaller inter-pillar distance, a gas–liquid interface must make more jumps through smaller throats in comparison with a zone with larger void-channels. Thus, the size of the inter-pillar pores and its throat-crest distribution has a major impact in the wetting efficiency. Besides, our results also agree with these of porous media in terms of the formation of viscous fingering, which is strongly related with the pore size gradient[58] and bed heterogeneity.[29]

Conclusions

In micro-packed beds the relative importance of surface forces over volume forces is high. Interactions on the boundaries between gas, liquid, and solid can determine the macroscopic flow patterns. We have explored which parameters are relevant in predicting fluid flow in micro-packed beds. We identify the following parameters that are often overlooked in trickle-bed literature: contact angle and inter-particle space. Our general conclusions are:

- For micro-packed beds the most relevant dimensionless number is the Capillary number (Ca). The surface tension-driven multiphase flow patterns are completely different to those in industrial and laboratory trickle bed reactors. The flow patterns encountered tend to exhibit segregation of the phases with high liquid hold-up values (>0.5). The gas–liquid interaction and the corresponding mass transfer rate can be boosted by increasing gas and liquid flow rates.
- Changing from a full wetting condition to a partial wetting condition produces a significant change in flow pattern. Under partial wetting conditions, random de-wetting of the solid surfaces takes place, decreasing the flow pattern stability. The gas–liquid–solid contact lines increase the flow resistance on a local level producing local liquid and pressure accumulation that conduce to liquid-slug formation.
- The size of void-channels has a major impact not only on the bed porosity, but also on the distribution of the phases inside the bed. With adequate dimensions for the distance between pillars, the gas–liquid interaction and the mass transfer rate can be tailored.
- It is still difficult to predict accurately the multiphase flow pattern for micro-packed and miniaturized packed beds because many variables (Ca number, contact angle, pore-connectivity, and feed-section design) are important. It is worthwhile to perform visualization and residence time distribution experiments in connection with hot flow experiments to establish the relation between bed packing characteristics and the gas–liquid–solid reaction performance as well as analysing trends with the parameters as reported here.

Our results point to the conclusion that controlling the multiphase flow pattern in micro-packed beds requires elucidating the following trinomial set of (a) fluids and Ca number in particular, (b) solid, with porosity and wetting as key factors and (c) bed geometry. The first two have been studied and modelled thoroughly in the literature, but innovative approaches are required to monitor the best solid geometry in the micro-chemical system.

Conflicts of interest

There are no conflicts to declare.

Acknowledgements

The authors thank Shell Global Solutions and Albemarle Catalysts Company for financial support.

References

1 K. F. Jensen, *AIChE J.*, 2017, **63**, 858–869.
2 K. S. Elvira, X. C. I. Solvas, R. C. R. Wootton and A. J. Demello, *Nat. Chem.*, 2013, **5**, 905–915.
3 A. C. Bédard, A. Adamo, K. C. Aroh, M. G. Russell, A. A. Bedermann, J. Torosian, B. Yue, K. F. Jensen and T. F. Jamison, *Science*, 2018, **361**, 1220–1225.
4 A. Günther and K. F. Jensen, *Lab Chip*, 2006, **6**, 1487–1503.
5 K. F. Jensen, *Chem. Eng. Sci.*, 2001, **56**, 293–303.
6 V. Hessel, P. Angeli, A. Gavriilidis and H. Löwe, *Ind. Eng. Chem. Res.*, 2005, **44**, 9750–9769.
7 M. W. Losey, R. J. Jackman, S. L. Firebaugh, M. A. Schmidt and K. F. Jensen, *J. Microelectromech. Syst.*, 2002, **11**, 709–717.
8 P. K. Plucinski, D. V. Bavykin, S. T. Kolaczkowski and A. A. Lapkin, *Catal. Today*, 2005, **105**, 479–483.
9 R. Halder and A. Lawal, *Catal. Today*, 2007, **125**, 48–55.
10 S. Tadepalli, R. Halder and A. Lawal, *Chem. Eng. Sci.*, 2007, **62**, 2663–2678.
11 F. Traschel, C. Hutter and P. Vonrohr, *Chem. Eng. J.*, 2008, **135**, 309–316.
12 S. McGovern, G. Harish, C. Pai, W. Mansfield, J. Taylor, S. Pau and R. Besser, *Chem. Eng. J.*, 2008, **135**, S229–S236.
13 H. P. L. Gemoets, Y. Su, M. Shang, V. Hessel, R. Luque and T. Noël, *Chem. Soc. Rev.*, 2016, **45**, 83–117.
14 M. N. Kashid and L. Kiwi-Minsker, *Ind. Eng. Chem. Res.*, 2009, **48**, 6465–6485.
15 M. K. Akbar, D. A. Plummer and S. M. Ghiaasiaan, *Int. J. Multiphase Flow*, 2003, **29**, 855–865.
16 P. Sobieszuk, J. Aubin and R. Pohorecki, *Chem. Eng. Technol.*, 2012, **35**, 1346–1358.
17 L. Yang, Y. Shi, M. Abolhasani and K. F. Jensen, *Lab Chip*, 2015, **15**, 3232–3241.
18 W. Ge, Q. Chang, C. Li and J. Wang, *Chem. Eng. Sci.*, 2019, **198**, 198–223.
19 Y. Wada, M. A. Schmidt and K. F. Jensen, *Ind. Eng. Chem. Res.*, 2006, **45**, 8036–8042.
20 S. Krishnamurthy and Y. Peles, *Phys. Fluids*, 2007, **19**, 043302.
21 B. A. Wilhite, K. F. Jensen, T. F. Hill, L. F. Velásquez-García, A. H. Epstein and C. Livermore, *AIChE J.*, 2008, **54**, 2441–2455.
22 S. Krishnamurthy and Y. Peles, *Chem. Eng. Technol.*, 2009, **35**, 55–65.
23 M. W. Losey, M. A. Schmnidt and K. F. Jensen, *Ind. Eng. Chem. Res.*, 2001, **40**, 2555–2562.
24 D. A. Hoang, C. Haringa, L. M. Portela, M. T. Kreutzer, C. R. Kleijn and V. van Steijn, *Chem. Eng. J.*, 2014, **236**, 545–554.
25 J. M. de Santos, T. R. Melli and L. E. Scriven, *Annu. Rev. Fluid Mech.*, 1991, **23**, 233–260.
26 I. A. Beresnev, W. Li and R. D. Vigil, *Transp. Porous Media*, 2009, **80**, 581–604.
27 M. Sharma, V. S. Reddy and A. A. Kulkarni, *Ind. Eng. Chem. Res.*, 2014, **53**, 1916–1923.
28 A. Gerami, Y. Alzahid, P. Mostaghimi, N. Kashaninejad, F. Kazemifar, T. Amirian, N. Mosavat, M. Ebrahimi Warkiani and R. T. Armstrong, *Transp. Porous Media*, 2018, **14**, 1–28.
29 A. Ferrari, J. Jimenez-Martinez, T. L. Borgne, Y. Méheust and I. Lunati, *Water Resour. Res.*, 2015, **51**, 1381–1400.
30 N. Márquez, P. Castaño, J. A. Moulijn, M. Makkee and M. T. Kreutzer, *Ind. Eng. Chem. Res.*, 2010, **49**, 1033–1040.
31 H. Khosravian, V. Joekar-Niasar and N. Shokri, *AIChE J.*, 2015, **61**, 1385–1390.
32 D. van Herk, P. Castaño, M. Makkee, J. A. Moulijn and M. T. Kreutzer, *Appl. Catal., A*, 2009, **365**, 199–206.
33 N. de Mas, A. Günther, T. Kraus, M. A. Schmidt and K. F. Jensen, *Ind. Eng. Chem. Res.*, 2005, **44**, 8997–9013.
34 N. Márquez, P. Castaño, M. Makkee, J. A. Moulijn and M. T. Kreutzer, *Chem. Eng. Technol.*, 2008, **31**, 1130–1139.
35 J. Zhong, A. Abedini, L. Xu, Y. Xu, Z. Qi, F. Mostowfi and D. Sinton, *Nanoscale*, 2018, **10**, 21994–22002.
36 S. R. A. de Loos, J. van der Schaaf, R. M. Tiggelaar, T. A. Nijhuis, M. H. J. M. de Croon and J. C. Schouten, *Microfluid. Nanofluid.*, 2010, **9**, 131–144.
37 V. Berejnov, N. Djilali and D. Sinton, *Lab Chip*, 2008, **8**, 689.
38 C. Roh, J. Lee and C. Kang, *Molecules*, 2016, **21**, 798.
39 W. Van der Merwe and W. Nicol, *Chem. Eng. Sci.*, 2009, **64**, 1267–1284.
40 P. Mohammadmoradi, S. Taheri, S. L. Bryant and A. Kantzas, *Chem. Eng. Sci.*, 2018, **191**, 300–317.
41 X. Yin, I. Zarikos, N. K. Karadimitriou, A. Raoof and S. M. Hassanizadeh, *Chem. Eng. Sci.*, 2019, **195**, 820–827.
42 CRC Handbook, *Handbook of Chemistry and Physics 99th Edition*, 2018.
43 G. M. Homsy, *Viscous Fingering in Porous Media*, Stanford Univ, Stanford, CA, USA, 1987, vol. 19.
44 R. Luo, Y. Chen and S. Lee, *Phys. Rev. Fluids*, 2018, **3**, 110502.
45 L. Yang, M. J. Nieves-Remacha and K. F. Jensen, *Chem. Eng. Sci.*, 2017, **169**, 106–116.
46 N. Marquez, M. Musterd, P. Castaño, R. Berger, J. A. Moulijn, M. Makkee and M. T. Kreutzer, *Chem. Eng. Sci.*, 2010, **65**, 3972–3985.
47 R. R. Kulkarni, J. Wood, J. M. Winterbottom and E. H. Stitt, *Ind. Eng. Chem. Res.*, 2005, **44**, 9497–9501.
48 J. Yue, G. Chen, Q. Yuan, L. Luo and Y. Gonthier, *Chem. Eng. Sci.*, 2007, **62**, 2096–2108.
49 N. Midoux, B. I. Morsi, M. Purwasasmita, A. Laurent and J. C. Charpentier, *Chem. Eng. Sci.*, 1984, **39**, 781–794.
50 P. G. de Gennes, F. Brochard-Wyart and D. Quéré, *Capillarity and Wetting Phenomena*, Springer New York, New York, NY, 2004.
51 R. Dreyfus, P. Tabeling and H. Willaime, *Phys. Rev. Lett.*, 2003, **90**, 144505.

52 T. Cubaud and C.-M. Ho, *Phys. Fluids*, 2004, **16**, 4575–4585.
53 K. Singh, M. Jung, M. Brinkmann and R. Seemann, *Annu. Rev. Fluid Mech.*, 2019, **51**, 429–449.
54 M. Serres, D. Schweich, V. Vidal and R. Philippe, *Chem. Eng. Sci.*, 2018, **190**, 149–163.
55 M. Serres, M.-L. Zanota, R. Philippe and V. Vidal, *Int. J. Multiphase Flow*, 2016, **85**, 157–163.
56 F. Arbabi, A. Kalantarian, R. Abouatallah, R. Wang, J. S. Wallace and A. Bazylak, *J. Power Sources*, 2014, **258**, 142–149.
57 A. Anbari, H.-T. Chien, S. S. Datta, W. Deng, D. A. Weitz and J. Fan, *Small*, 2018, **14**, 1703575.
58 H. S. Rabbani, D. Or, Y. Liu, C.-Y. Lai, N. B. Lu, S. S. Datta, H. A. Stone and N. Shokri, *Proc. Natl. Acad. Sci. U. S. A.*, 2018, **115**, 4833–4838.